THE JOURNAL OF PHYSICAL CHEMISTRY C

Article

Cite This: J. Phys. Chem. C XXXX, XXX, XXX−XXX

pubs.acs.org/JPCC

Exploring the Effect of Porous Structure on Thermal Conductivity in Templated Mesoporous Silica Films

Yan Yan,[†] Sophia C. King,[†] Man Li,[‡] Tiphaine Galy,[‡] Michal Marszewski,[‡] Joon Sang Kang,[‡] Laurent Pilon,[‡] Yongjie Hu,[‡] and Sarah H. Tolbert*[,†,§]

[†]Department of Chemistry and Biochemistry, University of California—Los Angeles, Los Angeles, California 90095-1569, United States

[‡]Department of Mechanical and Aerospace Engineering, University of California—Los Angeles, Los Angeles, California 90095-1597, United States

[§]Department of Materials Science and Engineering, University of California—Los Angeles, Los Angeles, California 90095-1595, United States

Supporting Information

ABSTRACT: This work elucidates the effect of porous structure on thermal conductivity of mesoporous amorphous silica. Sol−gel and nanoparticle-based mesoporous amorphous silica thin films were synthesized by evaporation-induced self-assembly using either tetraethyl orthosilicate or premade silica nanoparticles as the framework precursors with block copolymers Pluronic P123 or Pluronic F127 as template. The films were characterized with scanning- and transmission-electron microscopy, two-dimensional grazing-incidence small-angle X-ray scattering, ellipsometric porosimetry, and UV−vis reflectance spectroscopy. The thermal conductivity of the mesoporous films, at room temperature and in vacuum, was measured by time-domain thermoreflectance. The films were 150 to 800 nm thick with porosities ranging from 9% to 69%. Their pore diameters were between 3 and 19 nm, and their thermal conductivities varied between 0.07 and 0.66 W/m.K. The thermal conductivity decreased strongly with increasing porosity and was also affected by the structure of the silica framework (continuous or nanoparticulate) and the pore size. A simple porosity weighted effective medium approximation was used to explain the observed trend in thermal conductivity. These results give new insight into thermal transport in nanostructured materials, and suggest design rules of the nanoscale architecture to control the thermal conductivity of mesoporous materials for a wide range of applications.

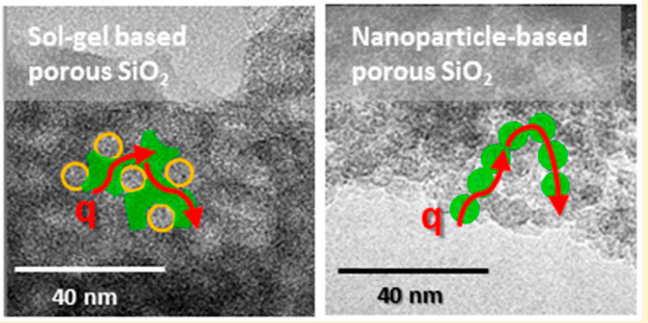

1. INTRODUCTION

Over the last few decades, mesoporous silica has been widely studied due to its simple synthesis and easily controlled structural properties. It is often used in a wide range of applications including thermally insulating materials, low-k dielectrics,[1,2] MEMS,[3,4] and window insulation.[5] Mesoporous silica is typically prepared by either template-free[6−10] or template-assisted synthesis.[11−14] In the template-free synthesis, random porosity is created by controlled gelation of dissolved molecular precursors and subsequent removal of the solvent. For instance, silica aerogels, prepared by supercritical drying of silica sol−gel without template, can reach porosities of 99%[15] and thermal conductivity of 0.013 W/m·K at room temperature and atmospheric pressure.[16] Similarly, silica ambigels can be synthesized by drying template-free silica precursors at ambient temperature and pressure. For example, Chang et al.[17] synthesized hydrophobic mesoporous silica by ambient drying and achieved a porosity of 97% and thermal conductivity of 0.034 W/m·K. However, due to high porosity and wide pore size distribution, silica aerogels and ambigels often do not have sufficient mechanical strength and/or optical transparency for a number of potential thermal barrier applications.[18]

By contrast, in template-assisted syntheses, the pores are formed by controlled gelation of molecular precursors around a template that is subsequently removed by physical or chemical treatment. Common templates include inorganic hard templates,[19,20] organic surfactants,[21,22] block copolymers,[23−26] and preformed polymer colloids.[27,28] In this approach, the pore volume and the pore size are easily controlled by choosing the amount and type of template so that pores can be kept small and homogeneous and scattering can be minimized, if needed. Several studies[29,30] report a thermal conductivity of 0.3−0.35 W/m·K at a porosity of ∼30% in templated porous silica.

Received: April 22, 2019
Revised: July 24, 2019

DOI: 10.1021/acs.jpcc.9b03767
J. Phys. Chem. C XXXX, XXX, XXX−XXX

Mesoporous silica has significantly lower thermal conductivity than bulk silica for several reasons.[30,31] First, the reduced volume of the solid phase reduces the heat conduction pathways. Second, the structural factors such as pore size and its distribution can also contribute to reduction in thermal conductivity of mesoporous silica, since the mean free path of heat carriers can be suppressed due to the boundary scattering near nanosized pores.[32−35] Finally, the interfacial resistance between nanodomains can also further decrease the effective thermal conductivity. Notably, the effects of these various nanostructural factors on the thermal conductivity of mesoporous silica has not been well documented to date.

Some examples of the existing data comes from Coquil et al.,[29] who reported the cross-plane thermal conductivity of highly ordered cubic and hexagonal mesoporous amorphous silica thin films synthesized by block copolymer templating methods. They found that the average thermal conductivity was 0.3 W/mK for silica films with cubic (3D interconnected) pore structure and 25% porosity and 0.2 W/mK for silica films with a hexagonal pore structure (linear pores) and 44% porosity. They concluded that the thermal conductivity decreases with increasing porosity and is independent of film thickness. This previous work found little variation with pore diameter and wall thickness, but the mesoporous silica films explored in that study all had porosity that fell in the relatively narrow range of 20−50%. More importantly, films with different pore symmetries could not be made with the same fractional porosity. Hopkins et al.[30] confirmed that mesoporous silica films prepared by templating methods had low thermal conductivity of around 0.3 W/mK at porosity around 25% percent, using time-domain thermoreflectance technique. Fang et al.[36,37] further compared thermal conductivity of mesoporous crystalline TiO_2 films prepared by a sol−gel synthesis and mesoporous TiO_2 films made from TiO_2 nanocrystals. They showed that the thermal conductivity of nanocrystal-based TiO_2 films was 40% lower than that of mesoporous TiO_2 films prepared by a sol−gel synthesis. They attributed these results to the facts that (1) the nanocrystal-based films had additional microporosity between TiO_2 nanocrystals, (2) the nanocrystals were smaller than the polycrystalline domains in the sol−gel films, and (3) the poorly connected nanocrystals caused significant phonon scattering at the interfaces between nanocrystals. These examples show that structural factors indeed play a significant role in heat transfer though mesoporous materials. Since it has recently been revealed from both experimental work and atomistic simulation that some heat carriers in amorphous silica have propagating features,[38,39] similar confinement phenomenon of heat carriers may also exist in mesoporous silica, despite its amorphous nature.

In this study, we further elucidate the effects of structural factors on thermal conductivity of mesoporous amorphous silica with specific emphasis on the effects of (1) porosity, (2) silica nanotexture (i.e., continuous vs particulate frameworks), and (3) pore size. A wide variety of sol−gel and nanoparticle-based mesoporous amorphous silica thin films are synthesized and characterized in terms of porosity, pore size, film thickness, and thermal conductivity. The results are analyzed and compared to the effective medium approximation model. Physical arguments are provided to relate the thermal conductivity of mesoporous silica to its nanoscale architecture.

2. EXPERIMENTAL SECTION

2.1. Materials. The following materials were obtained from commercial suppliers and used without further purification: colloidal suspension of SiO_2 nanoparticles (15 wt %, Nalco 2326, ammonia-stabilized colloidal silica, d = 5 nm, Nalco Chemical Company), triblock copolymer Pluronic P123 ($EO_{20}PO_{70}EO_{20}$, M_w = 5800 Da, BASF), triblock copolymer Pluronic F127 ($EO_{100}PO_{65}EO_{100}$, M_w = 12600 Da, BASF), tetraethyl orthosilicate (98%, Acros Organics), hydrochloric acid (Certified ACS Plus, Fisher Scientific), and ethanol (200 proof, Rossville Gold Shield).

2.2. Synthesis. Both sol−gel and nanoparticle-based mesoporous silica thin films were prepared by polymer templated evaporation-induced self-assembly (Scheme 1).

Scheme 1. Synthesis of Sol-Gel and Nanoparticle-Based Mesoporous Silica Films Produced via Evaporation Induced Self-Assembly, Using Pluronic Surfactants as Template and TEOS or Preformed Silica Nanoparticles as Inorganic Precursors

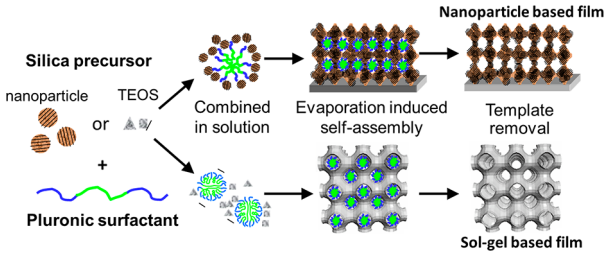

Tetraethyl orthosilicate (TEOS) was used as a silica precursor for the sol−gel films while premade silica nanoparticles were used as building blocks for the nanoparticle-based films. In both instances, triblock copolymers Pluronic P123 or Pluronic F127 were used as the structure-directing agents. The solution containing the precursors and the block copolymers was spin-coated on a silicon substrate. Upon evaporation, the system self-assembled into an organic−inorganic nanocomposite. Subsequently, the nanocomposite films were calcined to remove the block copolymer and develop the mesoporous structure.

Nanoparticle-Based Mesoporous Silica Films. First, a stock solution of polymer was made by dissolving 0.678 g of Pluronic P123 or Pluronic F127 in 3 mL deionized water. The stock polymer solution was then mixed with the colloidal suspension of SiO_2 nanoparticles to produce a solution with polymer/SiO_2 mass ratio m_{poly}/m_{SiO2} between 0.1 and 3 g/g. Then, 80 μL of the polymer−silica solution was spin-coated onto a 1 × 1 in^2 Si substrates. The film's thickness was adjusted by controlling the spin speed. The dried films were calcined in air at 350 °C for 30 min using 2 °C/min temperature ramp to remove the polymer. Nanoparticle-based silica powders were also synthesized from the same solutions for heat capacity measurements. Instead of spin-coating, these solutions were evaporated in a Petri dish at ambient condition for 1 day and collected in powdered form after calcination at 350 °C for 3 h in oxygen using a ramp rate of 5 °C/min for both heating and cooling. The powders were calcined for a longer time than the films to fully remove all of the polymer template from the micron scale grains of the powder sample. Since the calcination was done at such a low temperature, it is assumed that there was no significant difference in silica structure of the films and the powders.

DOI: 10.1021/acs.jpcc.9b03767
J. Phys. Chem. C XXXX, XXX, XXX−XXX

Sol–gel Based Mesoporous Silica Films. This method was adapted from the literature.[40] First, 25 mg of Pluronic F127 or Pluronic P123 was dissolved in 0.6 mL of ethanol and 0.16 mL of 0.05 M HCl. A certain amount of tetraethyl orthosilicate (TEOS) was added to the mixture to achieve a polymer to silica mass ratio m_{poly}/m_{SiO2} between 0.1 and 3. Then, 80 μL of the polymer–silica solution was spin-coated onto a 1 × 1 in^2 Si substrates. The film thickness was adjusted by controlling the spin speed. The dried films were calcined in air at 350 °C for 30 min using 2 °C/min temperature ramp to remove the polymer. Sol–gel silica powders were made from the same solutions for heat capacity measurements. Instead of spin-coating, the solutions were evaporated in a Petri dish at ambient condition for 1 day and collected in powdered form after calcination at 350 °C for 3 h in oxygen, again using a ramp rate of 5 °C/min for both heating and cooling. Here again, the powders were calcined for a longer time than the films to fully remove all of the polymer template from the micron scale grains of the powder samples. Since the calcination was done at such a low temperature, it is assumed that there was no significant difference in silica structure of the films and the powders.

2.3. Structural Characterization. Scanning Electron Microscopy (SEM) images were obtained using a model JEOL JSM-6700F field emission electron microscope with 5 kV accelerating voltage and secondary electron detector configuration. Transmission Electron Microscopy (TEM) images were obtained using a Technai G^2 TF20 High-Resolution EM, CryoEM and CryoET (FEI) at an accelerating voltage 200 kV and a TIETZ F415MP 16 megapixel 4k × 4k CCD detector. Two-dimensional grazing incidence small-angle X-ray scattering (2D-GISAXS) data were collected at the Stanford Synchrotron Lightsource (SSRL) using beamlines 1–5 with a wavelength of 0.1033 nm operated at an X-ray energy of 12.002 keV with a sample-to-detector distance of 2.870 m using a Rayonix-165 CCD detector. The data were then calibrated using silver behenate and reduced using the Nika package from Igor Pro.[41]

Ellipsometric porosimetry was performed on a PS-1100 instrument from Semilab using toluene as the adsorbate at ambient conditions to quantify porosity and pore size. The instrument used a UV–vis CCD detector adapted to a grating spectrograph to analyze the signal reflected by the sample. The light source was a 75 W Hamamatsu xenon lamp and the measurements were performed in the spectral range from 275–990 nm. Data analysis was performed using the associated Spectroscopic Ellipsometry Analyzer software assuming that the pores were cylindrical.

An optical reflectance based method was also used to verify the porosity and measure the film thickness. The experimental spectral normal-hemispherical reflectance $R_{exp,\lambda}$ was measured with a Shimadzu UV3101 PC UV–vis spectrophotometer equipped with a Shimadzu ISR3000 integrating sphere. The reference intensity was measured using a high specular reflection standard mirror by Ocean Optics (NIST certified STAN-SSH). The reflectance was measured in the visible range between 400 and 800 nm with a 1 nm spectral resolution. The porosity (ϕ) was then evaluated using a Maxwell-Garnett model using the refractive index ($n_{c,\lambda}$) retrieved from the reflectance measurement. The uncertainty of the retrieved porosity ($\Delta\phi$) was evaluated using the equation:

$$\Delta\phi = \sqrt{\left(\frac{\partial\phi}{\partial n_{eff,\lambda}}\Delta n_{aff,\lambda}\right)^2 + \left(\frac{\partial\phi}{\partial n_{c,\lambda}}\Delta n_{c,\lambda}\right)^2} \quad (1)$$

where the uncertainty of the refractive index of silica ($\Delta n_{c,\lambda}$) was calculated to be twice the standard deviation of $n_{c,\lambda}$ given by the Sellmeier formula over the 400–800 nm wavelength range.[42] This was found to be ($\Delta n_{c,\lambda}$) = 0.009 for all mesoporous silica films. The uncertainty, $\Delta n_{eff,\lambda}$, associated with the retrieved $n_{eff,\lambda}$ was found to be 0.003 for mesoporous silica films. Here, $\Delta n_{eff,\lambda}$ is defined as the average absolute difference between the refractive index used to predict the ideal spectral normal-hemispherical reflectance and the refractive index retrieved from the noisy normal-hemispherical reflectance.

2.4. Thermal Properties Characterization. Since the thickness of these mesoporous silica films was less than 1 μm, only a few thermal characterization techniques are suitable, including the 3ω method[29,43] and time-domain thermoreflectance (TDTR).[30,44] Considering the simpler fabrication processes and previously reported success of TDTR for extremely porous silica aerogel,[30] TDTR was used here for systematically investigating thermal conductivity of the various mesoporous silica films. Details of the TDTR setup are presented in Scheme 2. The detailed working principles and

Scheme 2. Experimental Setup for the Time-Domain Thermoreflectance (TDTR) Method Used for Thermal Conductivity Measurement on Mesoporous Silica Films on Si Substrate

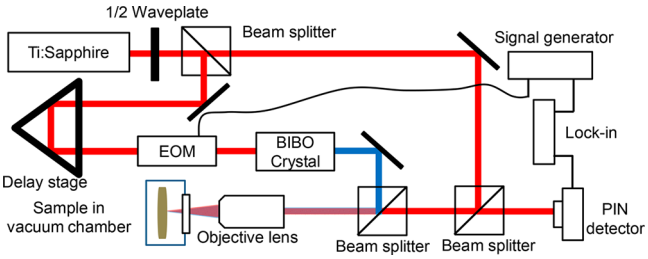

experimental setup can be found elsewhere.[45–48] In brief, a thin aluminum film (80 nm) was deposited by e-beam evaporation on the top surface of the samples. This film served as both a transducer to convert laser energy to thermal energy and a temperature sensor. The absorbed energy from the pump beam at 400 nm leads to an instantaneous temperature rise. The probe beam at 800 nm wavelength was used to continuously detect temperature decay by measuring reflectance using a photodiode. The delay time between pump pulse and probe pulse can be controlled with temporal resolution higher than subpicosecond. Next, the full transient decay curve from −100 to 5000 ps was fitted with a thermal diffusion model to obtain the thermal effusivity of the sample, which can be related to the thermal conductivity using the volumetric heat capacity.[44] To account for potential differences in the local thermal conductivity induced by variations in the nanoscale random network of silica, a large laser spot size of 20 μm in diameter was used. Similarly, to correct for the macroscale inhomogeneity of the mesoporous films and to ensure the reliability of the thermal conductivity data, TDTR measurements were repeated at 10 different locations on a 1 × 1 cm^2 surface area of the sample. Before all TDTR measurements, the samples were dehydrated by heating on a hot plate at 150 °C for more than 12 h. The thermal conductivity of the dehydrated samples was measured in a

DOI: 10.1021/acs.jpcc.9b03767
J. Phys. Chem. C XXXX, XXX, XXX–XXX

vacuum chamber with pressure less than 1 Pa at room temperature.

The specific heat capacity of the different mesoporous power silica samples of different porosities was measured using a Perkin-Elmer DSC 8000, a dual furnace differential scanning calorimeter equipped with an IntraCooler. This method was reported previously.[49] In brief, the samples were prepared in Al pans with vented covers to facilitate water loss at high temperatures. The specific heat capacity of each sample was measured using a step scan isothermal method from 20 to 30 °C with a 5 °C min^{-1} scan and 1.5 min hold at every 1 °C interval. The thermal conductivity of the films, κ, was retrieved from the thermal effusivity (e) obtained from TDTR and the c_p obtained from DSC using the equation:

$$\kappa_{\text{eff}} = \frac{e_{\text{eff}}^2}{C_{v,\text{eff}}} \tag{2}$$

Here, the volumetric heat capacity ($C_{v,\text{eff}}$) is estimated using the silica volume fraction ($\phi_{SiO_2} = 1 - \phi$), the silica density (ρ_{SiO_2}), and the measured specific heat capacity (c_{p,SiO_2}) of the silica samples as shown in the following:[49]

$$C_{v,\text{eff}} = \phi_{SiO_2}\rho_{SiO_2}c_{p,SiO_2} \tag{3}$$

The relative uncertainty of the thermal conductivity was then calculated as eq 4.

$$\frac{\Delta\kappa_{\text{eff}}}{\kappa_{\text{eff}}} = \sqrt{\left(\frac{\Delta e_{\text{eff}}^2}{e_{\text{eff}}^2}\right)^2 + \left(\frac{\Delta\phi_{SiO_2}}{\phi_{SiO_2}}\right)^2 + \left(\frac{\Delta c_{p,\text{eff}}}{c_{p,\text{eff}}}\right)^2} \tag{4}$$

Here, Δe_{eff}^2 was estimated as the standard deviation of a mean value of ten measurements, $\Delta\phi_{SiO_2} = \Delta\phi$, which was calculated using the method described in Section 2.3, and $\Delta c_{p,\text{eff}}$ was calculated based on the standard deviation of eight measured samples, four of which were nanoparticle-based and four of which were sol−gel based, as shown in the Supporting Information (SI) in Table S1.

3. RESULTS AND DISCUSSION

3.1. Structural Characterization. In this study, a wide variety of mesoporous silica thin films with different frameworks, porosities, and pore sizes were prepared to examine the effects of the nanoscale architecture on their thermal conductivity. The mesoporous silica thin films were prepared by evaporation induced self-assembly as previously described (Scheme 1). Different porosities, pore sizes, and wall thicknesses were achieved by varying the mass ratio of triblock copolymer template to silica.

Figure 1 shows typical SEM images of the sol−gel and nanoparticle-based mesoporous silica films. All films had well-developed mesoporosity with pore diameter ca. 10 nm throughout the structure and a smooth crack-free surface. The sol−gel based films displayed a more ordered porous structure with a continuous silica framework (Figure 1a) while the nanoparticle-based films had somewhat disordered pores and visible boundaries between the silica nanoparticles (Figure 1b).

To examine the local structure of the pore walls, we turn to transmission electron microscopy. Figure 2 shows TEM images of sol−gel and nanoparticle-based mesoporous silica films to illustrate the difference in frameworks between the two types of mesoporous materials. In the sol−gel mesoporous film (Figure 2a), the silica exists in a continuous molecular network where the wall thickness is fairly uniform and determined by both the pore size and porosity. In the nanoparticle-based film (Figure 2b), by contrast, individual silica nanoparticles are connected

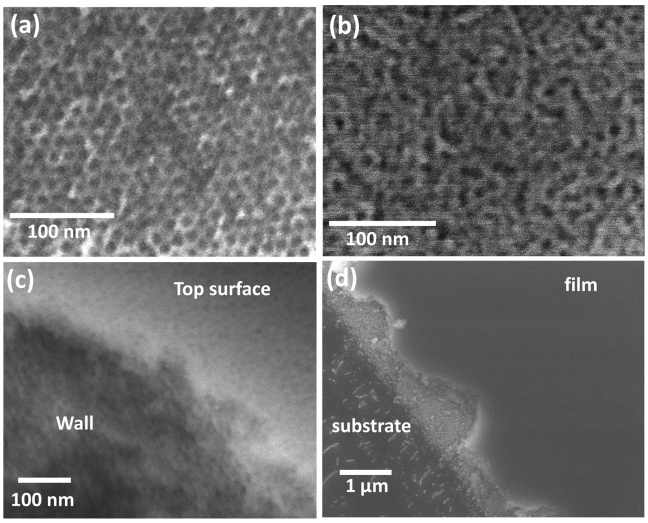

Figure 1. Typical scanning electron microscope images of mesoporous silica films. (a) Sol−gel based and (b) nanoparticle-based mesoporous silica films. (c) Zoomed in SEM of a cross-sectional of a razor blade cut in a nanoparticle-based mesoporous silica film showing homogeneous porosity through the film. (d) Zoomed out SEM of a mesoporous silica film on top of a Si substrate. Similar smooth, crack-free surfaces are observed for both sol−gel and nanoparticle-based silica films.

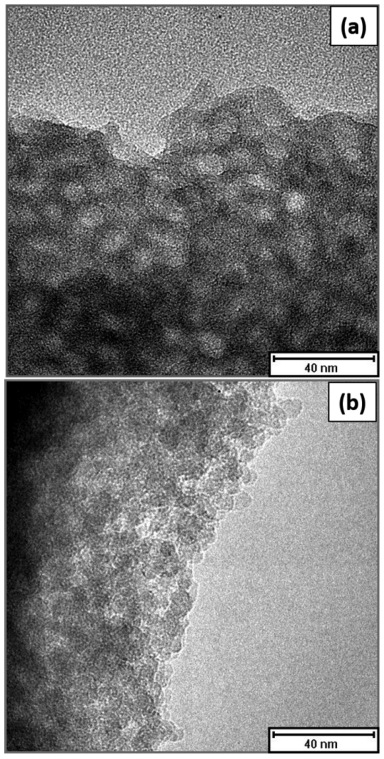

Figure 2. Transmission electron microscopy images of F127 templated (a) sol−gel and (b) nanoparticle-based mesoporous silica films. The images clearly show that the sol−gel network is continuously connected, while the nanoparticle-based films are composed of individual nanoparticles overlapping each other.

DOI: 10.1021/acs.jpcc.9b03767
J. Phys. Chem. C XXXX, XXX, XXX−XXX

and partially fused, with walls formed by one or multiple stacked nanoparticles.

Two-dimensional grazing-incidence small-angle X-ray scattering (2D-GISAXS) measurements were used to examine the mesoporous structure of the prepared films. Figure 3a and b

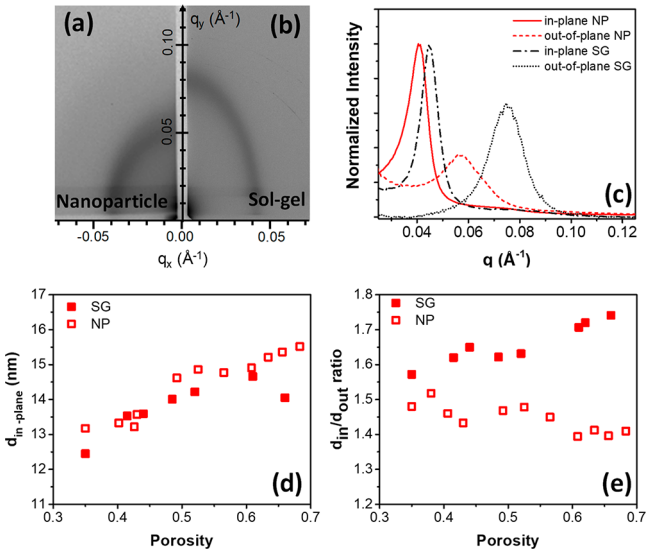

Figure 3. Small angle X-ray scattering of sol–gel (SG) and nanoparticle-based (NP) mesoporous silica films. A representative 2D-GISAXS pattern of a nanoparticle-based (a) and sol–gel based (b) mesoporous silica film. (c) Integrated intensity patterns converted from the 2D-GISAXS pattern along the q_x- and q_y-directions corresponding to in-plane and out-of-plane scattering for a typical sol–gel and nanoparticle-based films. (d) In-plane distance as a function of porosity and (e) ratio of in-plane distance/out-of-plane distance as a function of porosity for F127-templated sol–gel (SG) and nanoparticle-based (NP) films.

shows a representative 2D-GISAXS pattern of mesoporous nanoparticle based and sol–gel silica thin films, respectively. The diffraction arc along the q_x- and q_y- directions indicate that the films had ordered porosity both in the plane of the substrate and perpendicular to it. Figure 3b shows the integrated spectra from the 2D-GISAXS pattern of Figure 3a and b in both the in-plane (parallel to the substrate, q_x) and out-of-plane (perpendicular to the substrate, q_y) directions. Both in-plane and out-of-plane 2D-GISAXS featured a single diffraction peak indicating partly disordered porosity. These observations are consistent with the SEM images of the films (Figure 1). The in-plane diffraction peaks of both sol–gel and nanoparticle-based films had an intensity greater than twice that of the out-of-plane diffraction peak. This was due to the limited film thickness (<800 nm), which resulted in fewer scattering unit cells in the direction perpendicular to the substrate.

Film shrinkage during heat treatment could be seen by the fact that the in-plane scattering peak was at lower q than the out-of-plane peak. Since $q = 2\pi/d$, the interplane spacing d between repeating unit cells of mesopores along the direction perpendicular to the substrate was shorter than that in the direction parallel to the substrate. This indicates that during heat treatment the film shrank more in the direction perpendicular to the substrate than in the in-plane direction, which was pinned to the substrate, assuming that the as-synthesized film originally had isotropic pore spacing in all directions. The in-plane diffraction peak was observed in nearly all samples, while the out-of-plane diffraction peak was missing for samples with $m_{poly}/m_{SiO2} > 2$ and $m_{poly}/m_{SiO2} < 0.4$. For $m_{poly}/m_{SiO2} > 2$, the pores along the direction perpendicular to the substrate experienced extreme shrinkage during heat treatment due to the high porosity obtained for large m_{poly}/m_{SiO2} ratios. This extreme shrinkage destroyed the order along the q_y-direction resulting in the featureless 2D-GISAXS. On the other hand, for $m_{poly}/m_{SiO2} < 0.4$, the films were progressively thinner, with less repeat units, resulting in broader and weaker out-of-plane diffraction peak, until its complete disappearance.

Figure 3d compares the in-plane spacing, $d_{in\text{-}plane}$, calculated from the position of the in-plane diffraction peak for F127-templated sol–gel and nanoparticle-based mesoporous SiO_2 films with different porosities. The in-plane spacing, $d_{in\text{-}plane}$, increased almost linearly with the porosity for both sol–gel and nanoparticle-based films, which indicates that the pores, and likely the pore walls, grew larger with the increasing porosity. However, sol–gel and nanoparticle-based mesoporous silica films displayed different values and trends in the $d_{in\text{-}plane}/d_{out\text{-}of\text{-}plane}$ ratio as a function of porosity as shown in Figure 3e. In sol–gel based films, d_{in}/d_{out} ratio increased as porosity increased, as the films with higher porosity shrank more in the perpendicular direction to the substrate, leading to a smaller d_{out}. However, in nanoparticle-based films, the d_{in}/d_{out} ratio was relatively independent of porosity, likely because the preformed nanoparticle-based network underwent less shrinkage. Overall the d_{in}/d_{out} ratios at all porosities were higher in sol–gel based films than those in nanoparticle-based films due to the difference in shrinkage perpendicular to the substrate.

The porosity and pore size were further analyzed by ellipsometric porosimetry using toluene as an adsorbate.[50] Figure 4 shows adsorption/desorption isotherms and pore size distribution for sol–gel (Figure 4a) and nanoparticle-based (Figure 4b) silica films templated with Pluronic P123 for m_{poly}/m_{SiO2} = 1.5. Both isotherms were of type IV with H2(b)

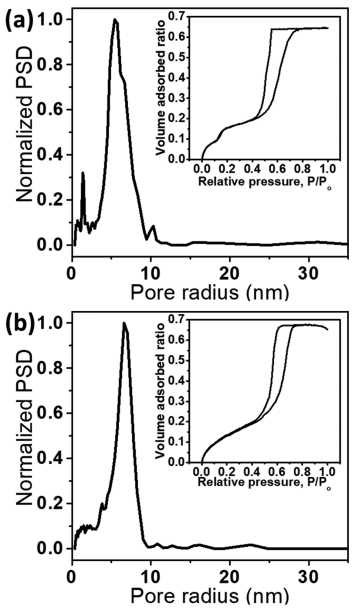

Figure 4. Typical pore size distributions (PSDs) and the corresponding adsorption–desorption isotherm obtained from ellipsometric porosimetry using toluene as the adsorbate at ambient conditions for (a) sol–gel and (b) nanoparticle-based silica thin films synthesized with a 1.5 g/g P123 to silica ratio.

DOI: 10.1021/acs.jpcc.9b03767
J. Phys. Chem. C XXXX, XXX, XXX–XXX

hysteresis loops according to the IUPAC classification.[51,52] Type IV isotherms demonstrate the presence of mesopores, with H2(b) hysteresis loops indicating a complex pore structure with some pore blocking.[53] The steep adsorption increase at high relative pressures, corresponding to capillary condensation in mesopores, suggests a fairly narrow pore size distribution.[54] This is consistent with the 2D-GISAXS patterns in Figure 3a and b, which indicate some periodicity in the samples, similar to more ordered counterparts such as the F127 templated cubic FDU-12 and P123 templated hexagonal SBA-15.[23,26,55] For these ordered materials, the derivative of the adsorption curve is often associated with the size of pore cages, while the desorption curve reports on constrictions or neck in the pores, but necessarily with less quantitative size information.[26] Both films had similar porosity (~65%) and similar adsorption pore sizes (10–14 nm). The sol–gel film also displayed a step in the isotherm at lower pressure ($P/P_o \approx 0.15$) that was not present in the nanoparticle-based films. The step corresponds to micropores with diameter ~3 nm created inside the mesopore walls by the block copolymer chains.[56,57]

Figure 5a and b summarizes the dependence of porosity on the polymer to silica mass ratio (m_{poly}/m_{SiO2}) in sol–gel and nanoparticle-based mesoporous silica films, respectively. The porosity in both sol–gel and nanoparticle-based films gradually increased up to 70% with increasing amount of polymer up to mass ratios $m_{poly}/m_{SiO2} > 2$. Further increase in m_{poly}/m_{SiO2} resulted in more shrinkage during heating instead of higher porosity. The sol–gel based silica system displays a wide range of porosity from 0% to 70% as any amount of polymer beyond the critical micelle concentration produced porosity in the final film. By contrast, the porosity of the nanoparticle-based films featured a lower limit around 35% due to the intrinsic porosity between randomly packed nanoparticles.

The average pore diameter of mesoporous silica films also increased with the increasing m_{poly}/m_{SiO2}, as shown in Figure 5c. This was in agreement with the increasing $d_{in\text{-}plane}$ spacing observed in the SAXS data. In addition, the average pore diameter was slightly larger in films templated with Pluronic F127 than in those templated with Pluronic P123, for a given m_{poly}/m_{SiO2} ratio. This was due to the larger molecular weight of Pluronic F127 (M_w = 12 700 Da) compared to Pluronic P123 (M_w = 5800 Da). We note that although the pore sizes for both sol–gel and nanoparticle-based films made from the same polymer template are similar at a given porosity, the distribution of wall thicknesses between the pores is not necessarily the same, since the precursors are different. Interestingly, despite the fact that the porosity no longer changed for $m_{poly}/m_{SiO2} > 2$ g/g, the average pore size continues to increase. Table S2 summarizes the porosity and film thickness of the various mesoporous silica thin films investigated in this work.

3.2. Thermal Conductivity Measurements. The key goal of this work is to correlate pore structure with thermal conductivity, and so in this section, we relate these various structural properties to the thermal conductivity, as measured by TDTR. Thermal conductivity data measured under vacuum is presented in Figure 6 below and listed in Table S2. Further discussion of this data and the trends can be found below.

Previous studies on thermal transport in mesoporous silica mostly focused on a narrow range of porosity.[29,30] Here, the thermal conductivity of mesoporous silica with a wide range of porosity was systematically studied. We also report, for the first time, the thermal conductivity of nanoparticle-based mesoporous silica films. Figure 6 shows the thermal conductivity as a function of porosity for both sol–gel based (Figure 6a) and nanoparticle-based (Figure 6b) mesoporous silica films. As

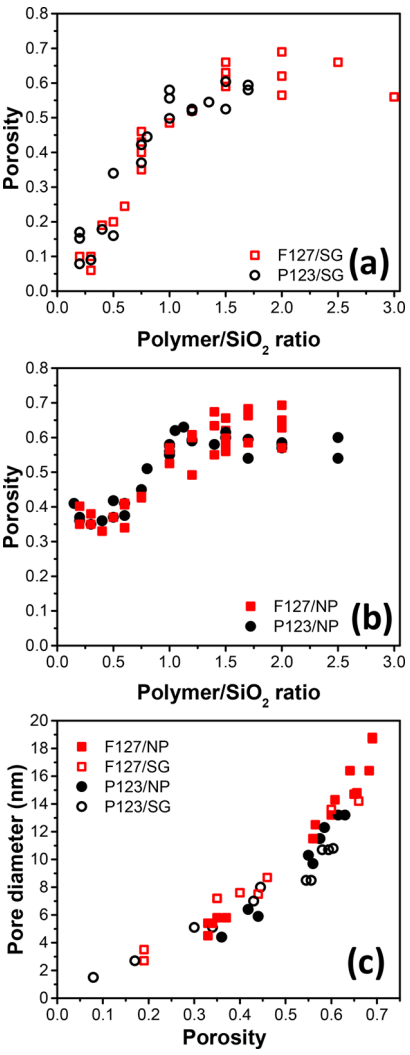

Figure 5. Porous structure characterized by ellipsometric porosimetry using toluene as the adsorbate at ambient conditions. Porosity as a function of polymer/silica ratio for (a) sol–gel (SG) and (b) nanoparticle-based (NP) mesoporous silica films. Samples were templated with either P123 or F127 block copolymers, as indicated on the figure. (c) Average pore diameter as a function of porosity in Pluronic surfactant-templated porous sol–gel and nanoparticle-based mesoporous silica films.

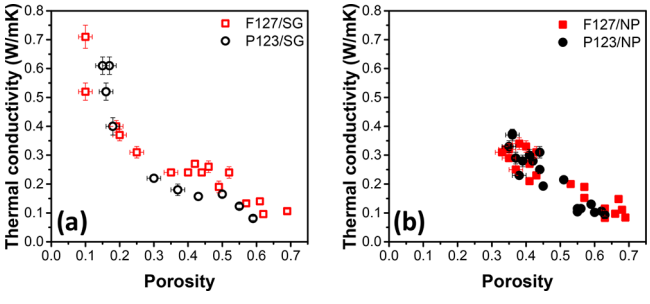

Figure 6. Thermal conductivity as a function of porosity for F127 and P123 templated (a) sol–gel (SG) silica and (b) nanoparticle-based (NP) silica mesoporous films measured under vacuum. No clear trends with the type of template used are observed, but there is a strong variation in thermal conductivity with porosity.

DOI: 10.1021/acs.jpcc.9b03767
J. Phys. Chem. C XXXX, XXX, XXX–XXX

expected, the thermal conductivity decreased with increasing porosity,[30,57] and thermal conductivities below 0.1 W/mK were achieved in both sol−gel and nanoparticle-based silica mesoporous films with porosities larger than 60%. Figure 6 also shows a stronger dependence of the thermal conductivity on the porosity in sol−gel mesoporous silica films compared with nanoparticle-based films, an observation that will be discussed further below.

In these amorphous porous materials, the heat is carried by nonpropagating vibrational modes whose coherent lengths should be much smaller than the silica wall thickness. In this case, an effective medium approximation (EMA) can be used to model the effect of porosity.[58] Figure 7 plots the thermal

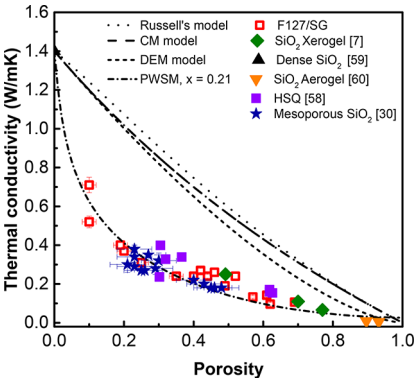

Figure 7. Thermal conductivity as a function of porosity for Pluronic F127 templated sol−gel silica films measured under vacuum, compared with a range of data for mesoporous silica reported in the literature[7,30,58−60] and several commonly used EMAs. Only the PWSM model accurately described the trends in the data.

conductivity of F127-templated sol−gel based mesoporous silica together with that of dense silica,[59] hydrogen-silsesquioxane (HSQ),[58] cubic and hexagonal mesoporous silica,[30] silica xerogel,[7] silica aerogel,[60] as well as predictions from several EMAs for the effective thermal conductivity of two phase media.[61] It is interesting to note that the thermal conductivity of the present mesoporous silica follows a similar porosity dependency to those previously reported despite major differences in synthesis and nanoscale architecture.

To understand the strong porosity dependence of the thermal conductivity, we first compared our data with EMAs based on classic heat conduction theory. For example, Russell's model was used for predicting the effective thermal conductivity κ_{eff} of bulk materials with spherical pores and is expressed as follows:[62]

$$\text{Russell's model } \kappa_{eff} = \kappa_{SiO_2}\frac{(1-\phi_p^{2/3})}{(1-\phi_p^{2/3}+\phi_p)} \quad (5)$$

where ϕ_p is the porosity and κ_{SiO_2} is the thermal conductivity of bulk silica. However, this prediction strongly overestimated the thermal conductivity of the different mesoporous silica, likely due to the major difference in morphology. The Clausius-Mossotti (CM) model and differential-effective-medium (DEM) theory have also been applied to predict the effective thermal conductivity of porous solid with ordered arrangement of identical pores[58] and are expressed as follows:

$$\text{CM model } \kappa_{eff} = \kappa_{SiO_2}\frac{(1-\phi_p)}{(1+0.5\phi_p)} \quad (6)$$

$$\text{DEM model } \kappa_{eff} = \kappa_{SiO_2}(1-\phi_p)^{1.5} \quad (7)$$

Unfortunately, both of these EMAs failed to capture the porosity dependence. Possible reasons include the fact that they ignore the pore shape, pore size, and the physical mechanisms responsible for energy transport in amorphous silica. Another model, which combines the classical series model with a parallel model $\kappa_{eff} = \kappa_{SiO_2}(1-\phi_p)$, called porosity weighted simple medium (PWSM) model has also been used to account for the porous structural parameters by using a fitting parameter x.[60] Considering the disperse phase in the pores to be vacuum, the PWSM simplifies to the following:[30]

$$\text{PWSM model } \kappa_{eff} = \kappa_{SiO_2}(1-\phi_p)(1-\phi_p^x) \quad (8)$$

Fitting the PWSM to our experimental measurements on F127-templated sol−gel films yielded $x = 0.21$, which is slightly larger than the value of $x = 0.17$ reported by Coquil et al.[27] The difference is likely due to the narrower range of porosity in the previous work (25−45%) compared to the present study (10−60%). Although it is difficult to physically interpret the meaning of x, this model is useful in predicting the thermal conductivity of mesoporous silica in the porosity range 10−60%.

The effects of solid framework morphology on the thermal transport in mesoporous silica was also explored by comparing the thermal conductivity of sol−gel and nanoparticle-based mesoporous silica films. For crystalline titania, these two morphologies showed very different results,[37] so it is interesting to see how they compare in an amorphous material like silica. As shown in Figure 8, although both kinds of mesoporous films

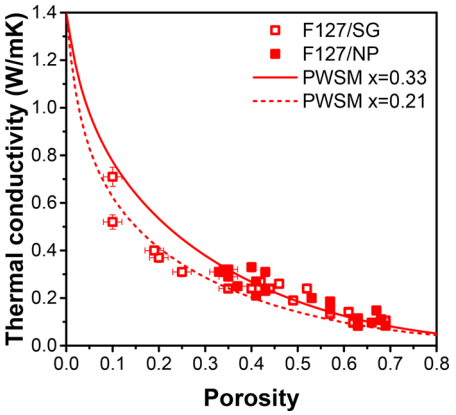

Figure 8. Thermal conductivity as a function of porosity for Pluronic surfactant templated sol−gel (SG) and nanoparticle-based (NP) mesoporous silica films measured under vacuum and fitted with the PWSM model. While both films show decreasing thermal conductivity with increasing porosity, the porosity dependence is influenced by the nanoscale architecture of the film.

feature decreasing thermal conductivity with increasing porosity, there are some observable differences. Near the lower porosity limit (~35%), the thermal conductivity of nanoparticle-based silica films was about 30% higher than that of sol−gel based films. However, for porosity above 45%, the difference in thermal conductivity between these two types of mesoporous frameworks became negligible. The PWSM model was fitted for each type of mesoporous silica thin films yielding $x = 0.21$ for sol−gel and $x = 0.33$ for nanoparticle-based silica mesoporous films. This suggests that the nanoparticle-based films offer more through-plane heat conduction pathways than

DOI: 10.1021/acs.jpcc.9b03767
J. Phys. Chem. C XXXX, XXX, XXX−XXX

the sol−gel films. In nanoparticle-based films, the size of the connections between nanoparticles should be mainly determined by the diameter of each silica nanoparticle and thus should be porosity independent. Since the size of the nanoparticles is uniform throughout the network, the heat conduction has equal probability to go along all joined nanoparticle chains, as modeled by the parallel model. In contrast, the sol−gel mesoporous films feature thin necks whose size decreases with decreasing pore size. The thin necks in the sol−gel networks should contribute significantly to the thermal resistance, resulting in low thermal conductivity in sol−gel mesoporous silica films at lower porosity.

Moreover, Figure 6a indicates that sol−gel based Pluronic F127-templated mesoporous silica films had a slightly higher thermal conductivity than those templated with P123. Since Pluronic F127 forms bigger micelles due its larger molecular weight, it typically forms larger pores. This suggests that sol−gel based silica films with smaller pore size have lower thermal conductivity. For a given porosity, smaller pore size is associated with thinner wall and thus should result in more scattering events for heat carriers at the boundaries of those walls. In contrast, nanoparticle-based silica films showed almost no effect of pore size on the thermal conductivity. This is most likely due to the fact that in the nanoparticle-based framework, scattering of heat carriers is dominated by the colloidal building blocks, rather than by the thickness of the walls.

4. CONCLUSIONS

This work presented synthesis, characterization, and cross-plane thermal conductivity measurements at room temperature of sol−gel and nanoparticle-based mesoporous amorphous silica thin films with various thicknesses, pore sizes, and porosities. The following conclusions can be drawn from the data presented here:

(1) Porosity plays a dominant role in lowering the thermal conductivity in both sol−gel and nanoparticle-based mesoporous silica films. The thermal conductivity depends nonlinearly on porosity. The average thermal conductivity of mesoporous silica films with porosity of 60% was measured as 0.1 ± 0.03 W/m·K at room temperature.

(2) The building block of the porous framework affects how thermal conductivity changes with porosity, with sol−gel films showing a steeper dependence on porosity than nanoparticle based films.

(3) For a given porosity, the thermal conductivity of sol−gel mesoporous silica decreases with decreasing pore size. This is likely due to thinner walls associated with smaller pores resulting in stronger scattering of heat carriers. The pore size has little effect on the thermal conductivity of nanoparticle-based mesoporous silica films, however, likely because the mean free path for thermal carriers is dominated by the nanoparticle itself, rather than the pore size.

Taken together, these results begin to paint a fuller picture of the roles of pore size, wall thickness, total porosity, and pore structure in determining the thermal conductivity of homogeneous, templated mesoporous silica materials.

ASSOCIATED CONTENT

Supporting Information

The Supporting Information is available free of charge on the ACS Publications website at DOI: 10.1021/acs.jpcc.9b03767.

The specific heat capacities used and details of the porosity, film thicknesses, and thermal conductivity of the thin film samples (PDF)

AUTHOR INFORMATION

Corresponding Author

*Phone: (310) 206-4767. E-mail: tolbert@chem.ucla.edu.

ORCID

Michal Marszewski: 0000-0002-4157-3046
Laurent Pilon: 0000-0001-9459-8207
Yongjie Hu: 0000-0001-7225-1130
Sarah H. Tolbert: 0000-0001-9969-1582

Notes

The authors declare no competing financial interest.

ACKNOWLEDGMENTS

We acknowledge the funding support from U.S. Department of Energy (DOE), Advanced Research Projects Agency-energy (ARPA-e) under Award Number DE-AR0000738. Author Y.Y. acknowledges fellowship support from the China Scholarship Council (CSC). The authors acknowledge the use of instruments at the Electron Imaging Center for NanoMachines supported by NIH (1S10RR23057) and the California NanoSystems Institute (CNSI) at UCLA. This manuscript contains X-ray diffraction data collected at the Stanford Synchrotron Radiation Lightsource. Use of the Stanford Synchrotron Radiation Lightsource, SLAC National Accelerator Laboratory, is supported by the U.S. Department of Energy, Office of Science, Office of Basic Energy Sciences, under Contract DE-AC02-76SF00515.

REFERENCES

(1) Maex, K.; Baklanov, M. R.; Shamiryan, D.; Lacopi, F.; Brongersma, S. H.; Yanovitskaya, Z. S. Low dielectric constant materials for microelectronics. *J. Appl. Phys.* **2003**, *93*, 8793−8841.

(2) Peercy, P. S. The drive to miniaturization. *Nature* **2000**, *406*, 1023.

(3) Veres, J.; Ogier, S. D.; Leeming, S. W.; Cupertino, D. C.; Mohialdin Khaffaf, S. Low-k insulators as the choice of dielectrics in organic field-effect transistors. *Adv. Funct. Mater.* **2003**, *13*, 199−204.

(4) Vigliante, A.; Kasper, N.; Brechbuehl, J.; Nolot, E. Applications of x-ray characterization for advanced materials in the electronics industry. *Metall. Mater. Trans. A* **2010**, *41*, 1167−1173.

(5) Powell, M. J.; Quesada-Cabrera, R.; Taylor, A.; Teixeira, D.; Papakonstantinou, I.; Palgrave, R. G.; Sankar, G.; Parkin, I. P. Intelligent multifunctional $VO_2/SiO_2/TiO_2$ coatings for self-cleaning, energy-saving window panels. *Chem. Mater.* **2016**, *28*, 1369−1376.

(6) Jain, A.; Rogojevic, S.; Ponoth, S.; Gill, W. N.; Plawsky, J. L.; Simonyi, E.; Chen, S.-T.; Ho, P. S. Processing dependent thermal conductivity of nanoporous silica xerogel films. *J. Appl. Phys.* **2002**, *91*, 3275−3281.

(7) Hu, C.; Morgen, M.; Ho, P. S.; Jain, A.; Gill, W. N.; Plawsky, J. L.; Wayner, P. C. Thermal conductivity study of porous low- *k* dielectric materials. *Appl. Phys. Lett.* **2000**, *77*, 145−147.

(8) Jin, C.; Luttmer, J. D.; Smith, D. M.; Ramos, T. A. Nanoporous silica as an ultralow-k dielectric. *MRS Bull.* **1997**, *22*, 39−42.

(9) Koebel, M.; Rigacci, A.; Achard, P. Aerogel-based thermal superinsulation: An overview. *J. Sol-Gel Sci. Technol.* **2012**, *63*, 315−339.

DOI: 10.1021/acs.jpcc.9b03767
J. Phys. Chem. C XXXX, XXX, XXX−XXX

(10) Deng, Z.; Wang, J.; Wu, A.; Shen, J.; Zhou, B. High strength SiO_2 aerogel insulation. *J. Non-Cryst. Solids* **1998**, *225*, 101−104.
(11) Eggiman, B. W.; Tate, M. P.; Hillhouse, H. W. Rhombohedral structure of highly ordered and oriented self-assembled nanoporous silica thin films. *Chem. Mater.* **2006**, *18*, 723−730.
(12) Alberius, P. C. A.; Frindell, K. L.; Hayward, R. C.; Kramer, E. J.; Stucky, G. D.; Chmelka, B. F. General predictive syntheses of cubic, hexagonal, and lamellar silica and titania mesostructured thin films. *Chem. Mater.* **2002**, *14*, 3284−3294.
(13) Lu, Y.; Ganguli, R.; Drewien, C. A.; Anderson, M. T.; Brinker, C. J.; Gong, W.; Guo, Y.; Soyez, H.; Dunn, B.; Huang, M. H.; Zink, J. I. Continuous formation of supported cubic and hexagonal mesoporous films by sol−gel dip-coating. *Nature* **1997**, *389*, 364.
(14) Zhao, D.; Feng, J.; Huo, Q.; Melosh, N.; Fredrickson, G.; Chmelka, B.; Stucky, G. Triblock co-polymer syntheses of mesoporous silica with periodic 50 to 300 angstrom pores. *Science* **1998**, *279*, 548−552.
(15) Hedrick, J. L.; Miller, R. D.; Hawker, C. J.; Carter, K. R.; Volksen, W.; Yoon, D. Y.; Trollsås, M. Templating nanoporosity in thin-film dielectric insulators. *Adv. Mater.* **1998**, *10*, 1049−1053.
(16) Venkateswara Rao, A.; Pajonk, G. M.; Haranath, D. Synthesis of hydrophobic aerogels for transparent window insulation applications. *Mater. Sci. Technol.* **2001**, *17*, 343−348.
(17) Wei, T.; Chang, T.; Lu, S.; Chang, Y. Preparation of monolithic silica aerogel of low thermal conductivity by ambient pressure drying. *J. Am. Ceram. Soc.* **2007**, *90*, 2003−2007.
(18) Jelle, B. P.; Baetens, R.; Gustavsen, A. Aerogel insulation for building applications. *Energy Build* **2011**, *43*, 761−769.
(19) Strubel, P.; Thieme, S.; Biemelt, T.; Helmer, A.; Oschatz, M.; Bruckner, J.; Althues, H.; Kaskel, S. ZnO hard templating for synthesis of hierarchical porous carbons with tailored porosity and high performance in lithium-sulfur battery. *Adv. Funct. Mater.* **2015**, *25*, 287−297.
(20) Schlottig, F.; Textor, M.; Georgi, U.; Roewer, G. Template synthesis of SiO_2 nanostructures. *J. Mater. Sci. Lett.* **1999**, *18*, 599−601.
(21) Cai, Q.; Lin, W.-Y.; Xiao, F.-S.; Pang, W.-Q.; Chen, X.-H.; Zou, B.-S. The preparation of highly ordered MCM-41 with extremely low surfactant concentration. *Microporous Mesoporous Mater.* **1999**, *32*, 1−15.
(22) Kresge, C. T.; Leonowicz, M. E.; Roth, W. J.; Vartuli, J. C.; Beck, J. S. Ordered mesoporous molecular sieves synthesized by a liquid-crystal template mechanism. *Nature* **1992**, *359*, 710−712.
(23) Zhao, D.; Sun, J.; Li, Q.; Stucky, G. D. Morphological control of highly ordered mesoporous silica SBA-15. *Chem. Mater.* **2000**, *12*, 275−279.
(24) Suzuki, K.; Ikari, K.; Imai, H. Synthesis of silica nanoparticles having a well-ordered mesostructure using a double surfactant system. *J. Am. Chem. Soc.* **2004**, *126*, 462−463.
(25) Smarsly, B.; Grosso, D.; Brezesinski, T.; Pinna, N.; Boissière, C.; Antonietti, M.; Sanchez, C. Highly crystalline cubic mesoporous TiO_2 with 10-nm pore diameter made with a new block copolymer template. *Chem. Mater.* **2004**, *16*, 2948−2952.
(26) Rauda, I. E.; Buonsanti, R.; Saldarriaga-Lopez, L. C.; Benjauthrit, K.; Schelhas, L. T.; Stefik, M.; Augustyn, V.; Ko, J.; Dunn, B.; Wiesner, U.; et al. General method for the synthesis of hierarchical nanocrystal-based mesoporous materials. *ACS Nano* **2012**, *6*, 6386−6399.
(27) Coquil, T.; Richman, E. K.; Hutchinson, N. J.; Tolbert, S. H.; Pilon, L. Thermal conductivity of cubic and hexagonal mesoporous silica thin films. *J. Appl. Phys.* **2009**, *106*, 1−11.
(28) Guillemot, F.; Brunet-Bruneau, A.; Bourgeat-Lami, E.; Gacoin, T.; Barthel, E.; Boilot, J. − P. Latex-templated silica films: Tailoring porosity to get a stable low-refractive index. *Chem. Mater.* **2010**, *22*, 2822−2828.
(29) Hatton, B.; Mishchenko, L.; Davis, S.; Sandhage, K. H.; Aizenberg, J. Assembly of large area, hightly ordered, crack-free inverse opal films. *Proc. Natl. Acad. Sci. U. S. A.* **2010**, *107*, 10354−10359.
(30) Hopkins, P. E.; Kaehr, B.; Phinney, L. M.; Koehler, T. P.; Grillet, A. M.; Dunphy, D.; Garcia, F.; Brinker, C. J. Measuring the thermal conductivity of porous, transparent SiO_2 films with time domain thermoreflectance. *J. Heat Transfer* **2011**, *133*, 61601.
(31) Smith, D. S.; Alzina, A.; Bourret, J.; Nait-Ali, B.; Pennec, F.; Tessier-Doyen, N.; Otsu, K.; Matsubara, H.; Elser, P.; Gonzenbach, U. T. Thermal conductivity of porous materials. *J. Mater. Res.* **2013**, *28*, 2260−2272.
(32) Lee, J.; Lim, J.; Yang, P. Ballistic phonon transport in holey silicon. *Nano Lett.* **2015**, *15*, 3273−3279.
(33) Yang, L.; Yang, N.; Li, B. Extreme low thermal conductivity in nanoscale 3d si phononic crystal with spherical pores. *Nano Lett.* **2014**, *14*, 1734−1738.
(34) Song, D.; Chen, G. Thermal conductivity of periodic micro-porous silicon films. *Appl. Phys. Lett.* **2004**, *84*, 687−689.
(35) Tang, G. H.; Bi, C.; Zhao, Y.; Tao, W. Q. Thermal transport in nano-porous insulation of aerogel: Factors, models and outlook. *Energy* **2015**, *90*, 701−721.
(36) Fang, J.; Reitz, C.; Brezesinski, T.; Nemanick, E. J.; Kang, C. B.; Tolbert, S. H.; Pilon, L. Thermal conductivity of highly-ordered mesoporous titania thin films from 30 to 320 K. *J. Phys. Chem. C* **2011**, *115*, 14606−14614.
(37) Coquil, T.; Reitz, C.; Brezesinski, T.; Nemanick, E. J.; Tolbert, S. H.; Pilon, L. Thermal conductivity of ordered mesoporous titania films made from nanocrystalline building blocks and sol-gel reagents. *J. Phys. Chem. C* **2010**, *114*, 12451−12458.
(38) Yang, L.; Zhang, Q.; Cui, Z.; Gerboth, M.; Zhao, Y.; Xu, T. T.; Walker, D. G.; Li, D. Ballistic phonon penetration depth in amorphous silicon dioxide. *Nano Lett.* **2017**, *17*, 7218−7225.
(39) Larkin, J. M.; McGaughey, A. J. H. Thermal conductivity accumulation in amorphous silica and amorphous silicon. *Phys. Rev. B: Condens. Matter Mater. Phys.* **2014**, *89*, 1−12.
(40) Dunphy, D. R.; Sheth, P. H.; Garcia, F. L.; Brinker, C. J. Enlarged pore size in mesoporous silica films templated by Pluronic F127: Use of poloxamer mixtures and increased template/SiO_2 ratios in materials synthesized by evaporation-induced self-assembly. *Chem. Mater.* **2015**, *27*, 75−84.
(41) Ilavsky, J. Nika: Software for two-dimensional data reduction. *J. Appl. Crystallogr.* **2012**, *45*, 324−328.
(42) Malitson, I. H. Interspecimen comparison of the refractive index of fused silica. *J. Opt. Soc. Am.* **1965**, *55*, 1205−1209.
(43) Cahill, D. G.; Goodson, K.; Majumdar, A. Thermometry and thermal transport in micro/nanoscale solid-state devices and structures. *J. Heat Transfer* **2002**, *124*, 223.
(44) Cahill, D. G. Analysis of heat flow in layered structures for time-domain thermoreflectance. *Rev. Sci. Instrum.* **2004**, *75*, 5119−5122.
(45) Li, M.; Kang, J. S.; Hu, Y. Anisotropic thermal conductivity measurement using a new asymmetric-beam time-domain thermoreflectance (AB-TDTR) method. *Rev. Sci. Instrum.* **2018**, *89*, 84901.
(46) Kang, J. S.; Wu, H.; Hu, Y. Thermal properties and phonon spectral characterization of synthetic boron phosphide for high thermal conductivity applications. *Nano Lett.* **2017**, *17*, 7507−7514.
(47) Kang, J. S.; Ke, M.; Hu, Y. Ionic intercalation in two-dimensional van der Waals materials: In-situ characterization and electrochemical control of the anisotropic thermal conductivity of black phosphorus. *Nano Lett.* **2017**, *17*, 1431−1438.
(48) Kang, J. S.; Li, M.; Wu, H.; Nguyen, H.; Hu, Y. Experimental observation of high thermal conductivity in boron arsenide. *Science* **2018**, *361*, 575−578.
(49) Marszewski, M.; Butts, D.; Lan, E.; Yan, Y.; King, S. C.; McNeil, P. E.; Galy, T.; Dunn, B.; Tolbert, S. H.; Hu, Y.; et al. Effect of surface hydroxyl groups on heat capacity of mesoporous silica. *Appl. Phys. Lett.* **2018**, *112*, 201903.
(50) Baklanov, M. R.; Mogilnikov, K. P.; Polovinkin, V. G.; Dultsev, F. N. Determination of pore size distribution in thin films by ellipsometric porosimetry. *J. Vac. Sci. Technol., B: Microelectron. Process. Phenom.* **2000**, *18*, 1385−1391.
(51) Haul, R.; Gregg, S. J.; Sing, K. S. W. Adsorption, surface area and porosity. *Berichte der Bunsengesellschaft für Phys. Chemie* **1982**, *86*, 957.
(52) Thommes, M.; Kaneko, K.; Neimark, A. V.; Olivier, J. P.; Rodriguez-Reinoso, F.; Rouquerol, J.; Sing, K. S. W. Physisorption of

DOI: 10.1021/acs.jpcc.9b03767
J. Phys. Chem. C XXXX, XXX, XXX−XXX

gases, with special reference to the evaluation of surface area and pore size distribution (IUPAC Technical Report). *Pure Appl. Chem.* **2015**, *87*, 1051−1069.
(53) Thommes, M.; Smarsly, B.; Groenewolt, M.; Ravikovitch, P. I.; Neimark, A. V. Adsorption hysteresis of nitrogen and argon in pore networks and charaterization of novel micro-and mesoporous silicas. *Langmuir* **2006**, *22*, 756−764.
(54) Kruk, M.; Jaroniec, M.; Ko, C. H.; Ryoo, R. Characterization of the porous structure of SBA-15. *Chem. Mater.* **2000**, *12*, 1961−1968.
(55) Fan, J.; Yu, C.; Gao, F.; Lei, J.; Tian, B.; Wang, L.; Luo, Q.; Tu, B.; Zhou, W.; Zhao, D. Cubic mesoporous silica with large controllable entrance sizes and advanced adsorption properties. *Angew. Chem., Int. Ed.* **2003**, *42*, 3146−3150.
(56) Ryoo, R.; Ko, C. H.; Kruk, M.; Antochshuk, V.; Jaroniec, M. Block-Copolymer-Templated Ordered Mesoporous Silica: Array of Uniform Mesopores or Mesopore−Micropore Network? *J. Phys. Chem. B* **2000**, *104*, 11465−11471.
(57) Tsui, B.-Y.; Yang, C.-C.; Fang, K.-L. Anisotropic thermal conductivity of nanoporous silica film. *IEEE Trans. Electron Devices* **2004**, *51*, 20−27.
(58) Costescu, R. M.; Bullen, A. J.; Matamis, G.; O'Hara, K. E.; Cahill, D. G. Thermal conductivity and sound velocities of hydrogen-silsesquioxane low-k dielectrics. *Phys. Rev. B: Condens. Matter Mater. Phys.* **2002**, *65*, 942051−942056.
(59) Cahill, D. G. thermal conductivity measurement from 30 to 750 K: The 3ω method. *Rev. Sci. Instrum.* **1990**, *61*, 802−808.
(60) Fricke, J.; Lu, X.; Wang, P.; Büttner, D.; Heinemann, U. Optimization of monolithic silica aerogel insulants. *Int. J. Heat Mass Transfer* **1992**, *35*, 2305−2309.
(61) Pietrak, K.; Winiewski, T. S. A review of models for effective thermal conductivity of composite materials. *Open Access J. J. Power Technol.* **2015**, *95*, 14−24.
(62) Russell, H. W. Principles of heat flow in porous insulators. *J. Am. Ceram. Soc.* **1935**, *18*, 1−5.

DOI: 10.1021/acs.jpcc.9b03767
J. Phys. Chem. C XXXX, XXX, XXX−XXX